Research Article Vol. 33, No. 21 / 20 Oct 2025 / *Optics Express* 44267

Optics EXPRESS

Intermodal four-wave mixing in silicon core fibers: enabling versatile wavelength conversion in the mid-infrared range

HAONAN REN,[1,*] MENG HUANG,[2] XINZE LIU,[1] AND ANNA C. PEACOCK[2]

[1] *Dalian University of Technology, School of Optoelectronic Engineering and Instrumentation Science, Dalian, 116024, China*
[2] *Optoelectronic Research Centre, University of Southampton, Southampton, SO17 1BJ, UK*
[*] *renhaonan@dlut.edu.cn*

Abstract: Highly nonlinear silicon core fibers (SCFs) that offer extended mid-infrared transmission provide a unique platform for efficient wavelength conversion within the 3-5 µm atmospheric window of use for free-space communications and remote sensing. Here, we numerically explore an intermodal four-wave mixing (FWM) scheme that allows for wide spectral translation using large, few-micron-sized-diameter SCFs, well-suited for transmitting the newly generated long-wavelength light. This scheme can be implemented in practical all-fiber devices using tapered nanospike couplers, enabling compact and integrated systems. Benefitting from the unique feature of intermodal zero dispersion, we predict that using only a 25 mm long SCF, it is possible to achieve wide conversion bandwidths (>300 nm) and very high efficiencies (2-15%) when pumped with a single fiber-based source at 1.95 µm. The all-fiber conversion scheme eliminates the need for bulky pump sources and mode converters, showcasing the unique advantages of SCFs for wide-ranging mid-infrared applications.

1. Introduction

Parametric nonlinear optical processes are widely exploited in numerous signal processing and quantum optical applications as they allow for frequency conversion of optical data signals with phase preservation [1–3]. These processes are generally classified into two categories based on the underlying nonlinear mechanism determined by the access to the second-order (χ^2) or third-order (χ^3) susceptibilities. Second-order nonlinear processes such as parametric down-conversion (PDC) are often associated with larger conversion efficiencies owing to the high χ^2 coefficients, but many of these systems rely on the use of bulk nonlinear crystals that hinder compact integration [4]. In contrast, four-wave mixing (FWM), a third-order nonlinear process, is highly compatible with integration schemes in both planar and fiber-based systems [5,6].

Over the past two decades, substantial progress has been made in realizing high-performance FWM demonstrations in both highly nonlinear silica-based fibers (HNLFs) and integrated silicon photonic waveguides [7–10]. While fiber-based devices offer a robust and low-loss interface to telecommunications systems, glass-based fiber devices can be bulky due to the extensive lengths required to achieve significant parametric gain, often ranging from meters to hundreds of meters. Furthermore, efficient parametric mixing necessitates meticulous dispersion management throughout the entire length of the fiber, particularly ensuring a stable zero-dispersion wavelength, which complicates fabrication and drives up costs.

In contrast, silicon photonics can offer high efficiencies over short lengths, and extensive studies of the phase-matching conditions have revealed the optimum FWM performance within

#575856 https://doi.org/10.1364/OE.575856
Journal © 2025 Received 7 Aug 2025; revised 25 Sep 2025; accepted 29 Sep 2025; published 10 Oct 2025

these integrated systems [11–14]. A complementary platform to the planar waveguides that has emerged recently is the silicon-core fibers (SCFs), as these can offer the benefits of the highly nonlinear silicon - two to three orders of magnitude higher than that of silica glass - inside a fiber geometry. Specifically, compared to conventional silicon-on-insulator (SOI) waveguides, SCFs offer radially symmetric mode field distributions that provide fundamentally different modal properties than rectangular planar waveguides. This supports excellent interconnection capabilities with standard fiber systems, addressing a key integration challenge for silicon photonic devices. Additionally, the larger core dimensions with higher numerical aperture (NA), scalable up to tens of micrometers, support a large number of guided modes with strong optical confinement, making SCFs particularly well-suited for mid-infrared applications where there is significant interest for free-space communications, environmental sensors, and imaging systems.

In particular, SCFs have been shown to support broadband supercontinuum generation up to wavelengths >5 µm, as well as FWM and Raman application beyond 2 µm [15,16]. However, extending the FWM capability to the mid-infrared window (3–5 µm) poses significant challenges. The dispersion characteristics of SCFs restrict the fundamental-mode FWM gain primarily to wavelengths close to the pump, necessitating that pump sources be as near to the 3–5 µm range as possible. The most commonly used fiber-based lasers, thulium-doped fiber lasers, can only provide wavelengths up to approximately 2 µm, resulting in a substantial spectral gap of over 1000 nm between the available pump wavelength and the desired 3–5 µm idler output. This considerable conversion span makes efficient fundamental-mode FWM for telecommunications-to-mid-infrared wavelength conversion unattainable.

In recent years, there has been growing interest in harnessing the multimode nature of optical fibers to overcome inherent limitations of single-mode systems. Fortunately, SCFs are inherently heavily multimode due to the large refractive index contrast between the silicon core ($n \approx 3.48$) and the silica cladding ($n \approx 1.44$), and a SCF with a 5 µm core diameter can support over a thousand of guided modes. Moreover, there have also been several successful demonstrations in harnessing the multimode nature of silicon systems to access a much wider array of phase-matching conditions through intermodal FWM, thus achieving broader wavelength conversion [9,17,18]. However, a distinct advantage of the SCFs over their planar counterparts is that the fibers can offer efficient conversion between the circularly symmetric mode profiles that have a high mode overlap [19], as has been demonstrated using multimode silica-based fiber systems [20–22]. Moreover, the SCFs are highly compatible with many 2 µm fiber lasers that are commonly used as pump sources for FWM applications targeting wavelength generation beyond 3 µm.

In this work, we use numerical simulations to investigate intermodal FWM in SCFs, targeting broadband frequency conversion into the mid-infrared spectral region. Our analysis reveals that the conversion efficiency (CE) of intermodal FWM is comparable to that of intramodal FWM using only the fundamental mode, while enabling the previously unattainable telecommunications-to-mid-infrared wavelength conversion. In a 5 µm core size SCF, we predict that it is possible to achieve broadband conversion bandwidths (>300 nm) and high efficiencies (2-15%, for fiber losses 0.2-1.2 dB/cm) assuming pumping by a thulium-doped fiber laser at 1.95 µm. Moreover, the pumping scheme can be simplified by using a tapered nanospike coupler, which facilitates simultaneous coupling of the LP_{01} and LP_{02} modes with only one pump source. This offers a pathway towards realizing fully fiberized telecommunications-to-mid-infrared parametric converters, where there is potential for use in application areas such as free-space optical communications and remote sensing.

2. Results and discussion

2.1. Silicon core fiber parameters

SCFs consist of a crystalline silicon core with a circular cross-section surrounded by a fused silica glass cladding, as shown in Fig. 1(a). They are typically fabricated in lengths of up to hundreds of meters using a modified fiber drawing approach based on the molten core drawing method [23]. Through post-processing techniques such as fiber tapering, propagation losses in the range of 0.2 dB/cm at telecom band can be routinely achieved, which is sufficiently low to observe significant nonlinear effects in lengths of less than 1 cm [15,24]. Fiber tapering can also be used to precisely adjust the core diameter from several micrometers down to hundreds of nanometers to alter the waveguide dispersion, which is required to achieve the desired phase-matching conditions for the FWM processes in different wavelength regions [25,26].

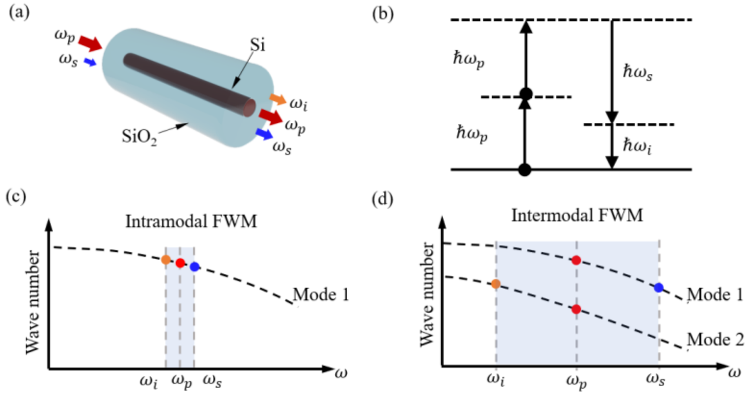

Fig. 1. (a) Schematic of the SCF structure supporting FWM. (b) Energy conservation diagram for pump wavelength degenerate FWM. (c) Phase-matching condition for intramodal FWM. (d) Phase-matching condition for intermodal FWM.

For FWM to occur in the SCFs, energy conservation requires the two pump photon energies must be equal to the sum of the signal and idler photon energies, as displayed in Fig. 1(b). At the same time, momentum conservation requires phase-matching of the effective wave numbers of the four interacting waves, which for the case of intramodal FWM (all waves in the same mode) can limit the conversion to narrow wavelength span, as shown in Fig. 1(c). However, if the FWM process is expanded to consider multiple modes such as the two-mode intermodal case shown in Fig. 1(d), a much greater conversion bandwidth can be achieved. In this study we focus on cases where the two pump beams have the same wavelength, but where they can exist in different modes as per the red dots in Fig. 1(d). In such cases only a single pump source is required, simplifying the practical implementation.

Due to the high refractive index contrast between the core and cladding, SCFs exhibit strong multimode behavior [19]. For a 5 μm core diameter SCF, the normalized frequency $V \approx 49$ at ~2 μm wavelengths, corresponding to over 1000 modes. Additionally, the weak birefringence inherent in silicon's cubic crystal structure results in these modes being polarization-independent. Analyzing all possible mode interactions in SCFs is challenging. To simplify the analysis, it is practical to focus on specific modes that are easier to manipulate experimentally and offer a strong overlap to facilitate efficient FWM processes. Despite the high refractive index contrast between the SCF core and cladding, we use the linearly polarized (LP) mode description for our study. This is justified as we are focusing on fibers with large core dimensions so that the effective indices of the degenerate vector modes are nearly identical, and the E_z component of the modal field can be neglected. The modal profiles of the first two circularly symmetric LP modes (LP$_{01}$, LP$_{02}$), which are most easily coupled to using on-axis launching conditions [19], are shown in Fig. 2(a) at representative wavelengths of 1.3 μm, 2 μm, and 5 μm in a 5 μm core diameter SCF. Despite this broad wavelength span, the modal field distributions exhibit remarkably similar characteristics, demonstrating negligible shape variations due to the strong confinement inherent in SCFs. Figure 2(b) shows the effective mode areas (A_{eff}) for both the LP_{01} and LP_{02} modes as a function of wavelength, confirming minimal variations across the wavelength range of interest. This similar characteristic is also generally valid for IR fibers based on heavy glasses like tellurite and chalcogenides used for ultra-broadband frequency conversion [27].

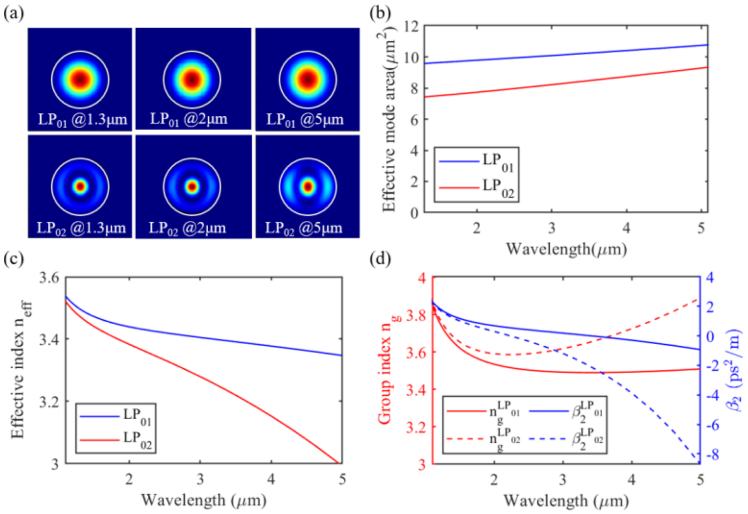

Fig. 2. (a) Mode profiles of LP_{01} and LP_{02} modes at wavelengths of 1.3 µm, 2 µm, and 5 µm in a 5 µm core diameter SCF. (b) Effective mode areas (A_{eff}) of LP_{01} and LP_{02} modes as a function of wavelength. (c) Effective refractive index versus wavelength for a 5 µm SCF. (d) Group index (left vertical axis) and second order dispersion (right vertical axis) across wavelength of interest.

The refractive index values for the silicon core and silica cladding are taken from Refs. [28,29]. Figure 2(c) presents the effective index (n_{eff}) for the two modes as calculated for a 5 µm core diameter SCF, specially designed for mid-infrared frequency conversion. The effective index difference between LP_{01} and the LP_{02} mode at a wavelength of 2 µm is approximately 0.05. In contrast, for silica-based fibers, this value can be as low as ~0.002 [10]. This large discrepancy arises from the substantial refractive index contrast between the silicon core and silica cladding in SCFs, which amplifies the differences in field overlap with the cladding between different modes. This characteristic is similarly reflected in the group index n_g and group velocity dispersion β_2. The zero-dispersion wavelengths (ZDWs) for the LP_{01} and LP_{02} modes are located at 3.5 µm and 2.25 µm, respectively, as illustrated in Fig. 2(d), highlighting the significant dispersion difference between the two modes. Additionally, the considerable variation in group index results in greater modal dispersion.

While our current implementation focuses exclusively on LP_{0x} modes, the broader potential of mode-mixing techniques remains to be explored. Although spatial light modulators enable arbitrary mode excitation, practical all-fiber mode coupling with high efficiencies are better aligned to the circularly symmetric modes, thereby rendering LP_{0x} modes the most promising for wavelength conversion applications. For interactions between the LP_{01} and LP_{02} modes, assuming degenerate pump wavelengths, there are 12 possible FWM combinations as listed in Table 1. Among these, intramodal FWM accounts for the case where all four waves propagate in either the LP_{01} or LP_{02} mode. For intramodal FWM, phase-matching is typically constrained to occur near the ZDW, determined by the dispersion curve of the respective mode. The remaining combinations represent intermodal FWM. We calculated the modal overlap factors for these cases using the definition provided in [30], as summarized in Table 1. These overlap factors are calculated from:

$$f_{1,2,3,4} = \frac{\iint F_1^* F_2 F_3 F_4^* dxdy}{\sqrt{\iint |F_1|^2 dxdy \iint |F_2|^2 dxdy \iint |F_3|^2 dxdy \iint |F_4|^2 dxdy}}, \tag{1}$$

where F_1 and F_2 are the spatial mode field distribution of the pump at pumping wavelength, F_3 and F_4 are the spatial mode field distribution of the signal and idler at operation wavelength. Moreover, we use normalized overlap factors $f'_{1,2,3,4}$ to provide a more intuitive comparison of different mode combinations relative to the intramodal case as $f'_{1,2,3,4} = \bar{A}_{eff}/\sqrt{n_1 n_2/n_3 n_4} f_{1,2,3,4}$, where $\bar{A}_{eff}$ is the geometric mean of the effective area for both pumps, n_1, n_2 are the effective mode index of the pumps and n_3, n_4 are the effective mode index of the signal and idler.

Table 1. Normalized Overlap Factors for FWM Combinations Between LP_{01} and LP_{02} Modes. Pump waves at 1.95 µm, signal at 1.3 µm, and idler at 3.9 µm.

Pump 1	Pump 2	Signal	Idler	Overlap	Type
LP_{01}	LP_{01}	LP_{01}	LP_{01}	1	Intra modal
		LP_{01}	LP_{02}	0.87	Inter modal
		LP_{02}	LP_{01}	0.81	
		LP_{02}	LP_{02}	0.85	
LP_{01}	LP_{02}	LP_{01}	LP_{01}	0.72	
		LP_{01}	LP_{02}	0.75	
		LP_{02}	LP_{01}	0.75	
		LP_{02}	LP_{02}	0.87	
LP_{02}	LP_{02}	LP_{01}	LP_{01}	0.66	
		LP_{01}	LP_{02}	0.77	
		LP_{02}	LP_{01}	0.78	
		LP_{02}	LP_{02}	0.97	Intra modal

In our calculations for Table 1, we accounted for wavelength-dependent mode profiles: the pump mode profile is calculated at 1.95 µm, with the signal mode at 1.3 µm and idler mode at 3.9 µm. The fiber core diameter is fixed for 5 µm. For other signal and idler wavelengths, the overlap factors have minimal fluctuation due to the strong modal confinement of SCF. For example, in an intermodal configuration (pumps in LP_{01} and LP_{02}, signal in LP_{01}, and idler in LP_{02}), the overlap factor varies by merely 2.5% (from 0.76 to 0.74) when signal/idler wavelengths range across 1.2-1.44 µm/3-5 µm.

2.2. Mode coupler design for all-fiberized intermodal FWM

All-fiberized devices are low-cost, compact, and robust, eliminating the need for bulk coupling lenses. However, a significant practical challenge in realizing an all-fiberized intermodal FWM system is selectively exciting fiber modes while preserving the all-fiber architecture. This requires coupling of the pump into the SCFs without introducing free space components such as spatial light modulators. To address this challenge, we utilize an inverse taper coupler structure that enables the simultaneous excitation of the LP_{01} and LP_{02} modes while also facilitating seamless fusion splicing between the SCF and a standard single-mode fiber (SMF) delivering the pump laser. The SCF inverse taper coupler, also referred to as the nanospike coupler in SCFs, was first proposed in 2017 [31]. These couplers can be formed directly when the SCFs are tapered down to tens of micrometer outer dimensions such that the silicon core gradually disappears as the cladding collapses, forming a spike shape. The tip of the nanospike is less than 50 nm in size, which is small enough to allow the mode from the silicon core to leak into the silica cladding, where it is guided by the cladding-air structure. Mostly, these nanospike couplers have been used for fundamental mode coupling by using long coupling lengths to support an adiabatic transition. However, by using slightly shorter lengths, we have found that these structures can also support coupling to the LP_{02} mode. Thus, by utilizing a single tapered nanospike coupler at the input, light can be coupled into both the LP_{01} and LP_{02} modes of the SCF simultaneously, enabling a single pump to trigger the intermodal FWM process.

The focus of this work is the generation of mid-infrared idler waves for applications in the 3–5 μm region. Thus the pump source is modelled based on a thulium-doped tunable fiber laser operating over the range 1.9-2 μm and the signal is based on an O-band semiconductor laser at ~1.3 μm [32]. As illustrated in the schematic of Fig. 3(a-b), the pump and signal could be combined using a wavelength division multiplexer (WDM) and coupled into a short section of SCF via the nanospike coupler connected to an SMF that has been tapered to match the outer diameter of the SCF, as described in Ref. [31]. This allows for the modes to transfer seamlessly within the silica cladding, before coupling into the core of the SCF through the sharp, nanometer-sized silicon tip. Most of the light is coupled into the LP_{01} mode of the SCF, with a smaller portion can be coupled into the LP_{02} mode, ensuring both pump and signal waves undergo mode conversion.

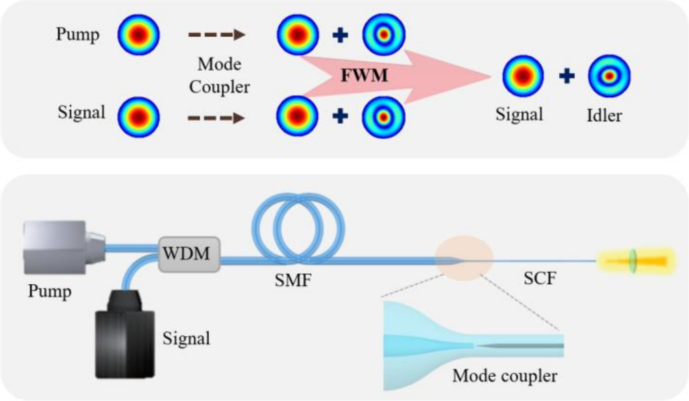

Fig. 3. (a) Schematic of the intermodal FWM system based on a tapered nanospike coupler. Initially, the pump and signal are in the fundamental mode (LP_{01}), which are then converted to LP_{01} and LP_{02} modes via the nanospike coupler at the SCF input. The FWM process occurs in the SCF section, generating an idler wave in the LP_{02} mode. (b) Proposed setup for the all-fiber mid-infrared laser system. The fiber-coupled pump and signal are combined via a WDM, transmitted through an SMF segment, and coupled into the nanospike coupler via a tapered SMF fusion splice.

After passing through the coupler region, the light will propagate through the section of untapered SCF with a core size of 5 μm, as selected for optimized phase-matching. As mid-infrared wavelengths cannot be coupled back into SMF due to the high absorption of silica at these wavelengths, we propose a free-space output coupling scheme. Such an approach would maintain the all-fiber architecture for pump and signal coupling, while enabling efficient generation and free-space extraction of the mid-infrared light for practical applications. The coupling loss for the output end can be primarily attributed to Si-air reflection (0.8 dB) and mode overlap mismatch (0.4 dB) between the fiber and collection optics, assuming using a 5 μm core SCF with a NA = 0.85 mid-infrared lens. The coupling loss at the input end is primarily due to the coupling ratio to the cladding mode of the SCF, which is strongly influenced by the input field area. The smaller the cladding diameter of the SCF at the fusion joint with the silica fiber, the lower the coupling loss. A coupling loss of 4 dB has been reported experimentally for a cladding diameter of 30 µm; however, this loss can be reduced to 0.5 dB when the fiber cladding is minimized to 10 µm [31].

Owing to the wide wavelength separation, the signal and pump waves exhibit different coupling efficiencies into the LP_{01} and LP_{02} modes, which depend on the length of the nanotaper design. These mode coupling efficiencies were calculated using finite-element eigenmode expansion (EME) solver, where the input end receives the fundamental mode from a tapered single mode fiber. The SCF nanospike structure features a tip diameter of 50 nm, a variable taper length, and terminates in a 1 µm diameter end facet forming an elongated conical region. To illustrate this, Fig. 4(a) shows calculations of the mode coupling ratios as a function of taper length for a nanospike structure with a 10 µm cladding at the coupling facet. The results show that a 1.95 µm LP_{01} pump wave from silica fiber can achieve 83% coupling efficiency in the LP_{01} mode and 14% efficiency in the LP_{02} mode when the taper length is 200 µm. This coupling process is shown in Fig. 4(c). In contrast, a signal wave positioned at 1.3 µm has a coupling efficiency of 47% in the LP_{01} mode and 24% in the LP_{02} mode. Figure 4(b) illustrates the relationship between the coupling efficiency and wavelength for the LP_{01} and LP_{02} modes when the taper length is 200 µm. It is evident that there is a significant correlation with wavelength.

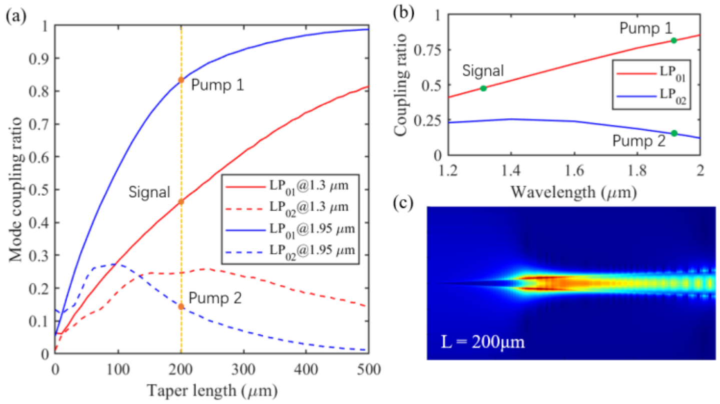

Fig. 4. Calculated coupling performance of the nanospike taper coupler. The SCF nanospike structure features a 10 µm cladding diameter, a tip diameter of 50 nm, terminates in a 1 µm diameter end facet, and has a taper length of L. The input is from a 10 µm air-clad silica fiber. (a) Coupling efficiency as a function of taper length for specific operating wavelengths (as labeled in the legend). (b) Coupling efficiency to LP_{01} and LP_{02} modes as a function of wavelength from 1.2-2 µm for a fixed spike length of 200 µm. (c) Calculated intensity distribution of mode field transmission for a spike length of 200 µm, wavelength of 1.95 µm.

We note that the remaining light is expected to couple into higher-order modes or cladding modes before being scattered out. The coupling ratios for different modes in the nanospike can also be adjusted by varying the taper length or changing the input mode type. For example, by using a tapered multimode fiber as the input end and launching the LP_{02} mode as input, the LP_{02} mode of the SCF can be excited more efficiently.

2.3. Conversion efficiency of SCF

In the proposed intermodal FWM process, two identical wavelength photons ω_1 and ω_2 from separate pump waves, propagating in LP_{01} and LP_{02} modes respectively, are converted to a signal photon ω_3 and an idler photon ω_4. The generated signal photons amplify the incident signal beam, while the idler photons generate a beam at a new frequency. Efficient FWM processes occur when both energy conservation and momentum conservation are satisfied. Energy conservation is expressed as:

$$\omega_1 + \omega_2 = \omega_3 + \omega_4. \tag{2}$$

In our proposed scheme for mid-infrared generation, both pumps operate at 1.95 μm ($\omega_1 = \omega_2$) while the signal is positioned near ~1.3 μm, correspond to an idler wave near ~3.9 μm. Conservation of momentum is more challenging and requires minimal phase mismatch between the four waves. The effective phase mismatch Δk comprises both linear and nonlinear contributions:

$$\Delta \mathrm{k} = \Delta \mathrm{k}_{\mathrm{L}} + \Delta \mathrm{k}_{\mathrm{NL}}. \tag{3}$$

The linear phase mismatch is governed by the fiber design and operation wavelength, and is given by:

$$\Delta \mathrm{k}_{\mathrm{L}} = \frac{n_3\omega_3}{c} + \frac{n_4\omega_4}{c} - \frac{n_1\omega_1}{c} - \frac{n_2\omega_2}{c}, \tag{4}$$

where c is the speed of light in vacuum. The nonlinear phase mismatch in multimode fiber four-wave mixing is expressed as a linear combination of the two pump powers with nonlinear coefficients:

$$\Delta \mathrm{k}_{\mathrm{NL}} = P_1\gamma_{\mathrm{eff1}} + P_2\gamma_{\mathrm{eff2}}, \tag{5}$$

where P_1 and P_2 are the corresponding pump powers, and γ_{eff1} and γ_{eff2} are the real part of effective nonlinear coefficients for the respective pumps. The effective nonlinear coefficients for pump1 and pump2 accounts for all relevant self-phase modulation (SPM) and cross-phase modulation (XPM) contributions between different modes, and is described as [33]:

$$\gamma_{\mathrm{eff1}} = 2\delta_3 f_{31} + 2\delta_4 f_{41} - 2\delta_2 f_{21} - \delta_1 f_{11}, \tag{6}$$

$$\gamma_{\mathrm{eff2}} = 2\delta_3 f_{32} + 2\delta_4 f_{42} - 2\delta_1 f_{12} - \delta_2 f_{22}, \tag{7}$$

where $f_{mn} = \iint F_1^* F_2 dxdy / \sqrt{\iint |F_1|^2 dxdy \iint |F_2|^2 dxdy}$, represents the mode overlap integral between modes m and n, which quantifies the spatial overlap of the electric field distributions. δ_i is defined as $\delta_i = 2\pi\bar{n}_2/\lambda_i$, where $\bar{n}_2$ is the Kerr coefficient.

Figure 5(a) shows the calculated intermodal phase-matching as a function of signal wavelength for a 50:50 power distribution ($P_1 = P_2 = 10\mathrm{W}$, $\bar{n}_2 = 9 \times 10^{-18} \mathrm{m}^2/\mathrm{W}$ [34], core diameter $d = 5$ μm, pump1, pump2, signal and idler are in LP_{01}-LP_{02}-LP_{01}-LP_{02}). Near the pump wavelength of 1.95 μm, there exists a zero dispersion point where Δk remains close to zero for a wide signal/idler wavelength range. This result introduces the novel concept of intermodal zero dispersion, which represents a significant discovery that distinguishes our work from previous studies. The ratio between the two pump powers can influence the gain coefficient, with maximum gain achieved when both pumps have equal power.

To accurately model intermodal FWM in SCFs, we have included a comprehensive coupled-wave equation framework in the Appendix that incorporates both linear losses and nonlinear effects such as two-photon absorption (TPA) and free-carrier absorption (FCA). However, these equations are complex and lack analytical solutions, requiring numerical methods for computation. Thus, to gain an intuitive understanding of the process, we start by adopting a simplified analytical approach where TPA and linear losses are neglected. The validity of this approximation is helped by the large SCF core sizes and the low TPA parameters of the pump wavelengths considered in our analysis, and by considering low pump intensities over short propagation distances. Thus, we derive closed-form analytical expressions (see Appendix) for the phase-matching dependence on

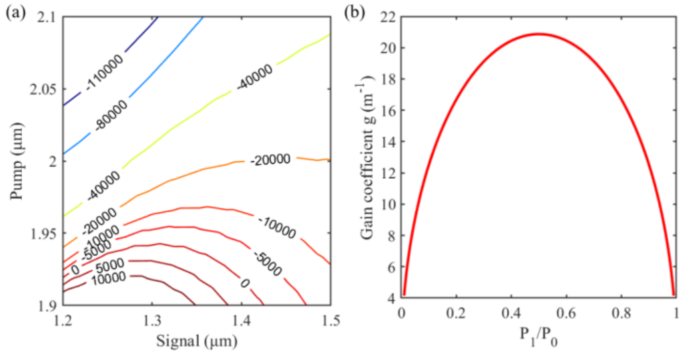

Fig. 5. (a). Effective phase mismatch Δk (m^{-1}) as a function of both signal and idler wavelength for a 5 μm core diameter SCF. (b). Parametric gain g as a function of pump power ratio in the LP_{01} mode to total pump power.

the signal and idler evolution equations as:

$$\frac{\partial A_3}{\partial z} = i\delta_3[2f_{1234}A_1A_2A_4^* \exp(-i\Delta kz)], \tag{8a}$$

$$\frac{\partial A_4}{\partial z} = i\delta_4[2f_{1234}A_1A_2A_3^* \exp(-i\Delta kz)]. \tag{8b}$$

Here, A_1, A_2, A_3, A_4 are the complex amplitudes of the two pump waves, signal wave, and idler wave respectively, z is the propagation distance along the fiber. Thus, the wavelength dependent modal properties primarily influence the signal and idler propagation through the terms $\delta_i f_{1234}$ and Δk_{NL}. The signal and idler expression are obtained after rigorous and standardized mathematical procedures for solving Eq. (8) [35,36]:

$$P_3(z) = P_3(0)\left[1 + \left(\frac{\gamma_{FWM}\sqrt{P_1P_2}}{g}\right)^2 \sinh^2(gz)\right], \tag{9a}$$

$$P_4(z) = P_3(0)\left(\frac{\gamma_{FWM}\sqrt{P_1P_2}}{g}\right)^2 \frac{\delta_4}{\delta_3}\sinh^2(gz), \tag{9b}$$

where γ_{FWM} is the real part of effective nonlinear coefficient for the intermodal FWM process:

$$\gamma_{FWM} = \sqrt{\delta_3\delta_4}f_{1234}, \tag{10}$$

and g is the parametric gain coefficient:

$$g = \sqrt{\left(\gamma_{FWM}\sqrt{P_1P_2}\right)^2 - \left(\frac{\Delta k}{2}\right)^2}. \tag{11}$$

The parametric gain coefficient g provides a comprehensive description of the intermodal FWM signal and idler evolution, incorporating both linear phase mismatch and nonlinear coupling effects. This model is equivalent to modulation instability analysis in the small-signal regime, as both phenomena originate from the same underlying process. The parametric gain approach offers practical advantages for device design by directly relating pump power distribution and phase-matching conditions to CE, enabling systematic optimization of modal configurations and wavelength selection for enhanced FWM performance. From Eq. (9), we can obtain the CE between signal and idler as:

$$CE = \frac{P_4(z)}{P_3(0)} = \left(\frac{\gamma_{FWM}\sqrt{P_1P_2}}{g}\right)^2 \frac{\delta_4}{\delta_3}\sinh^2(gz), \tag{12}$$

According to the Eq. (12), CE is determined by the combined effects of the geometric mean pump power $\sqrt{P_1P_2}$, the nonlinear coefficient γ_{FWM} and the phase mismatch Δk. The key distinction from intramodal FWM lies in that both nonlinear coefficient and Δk are influenced by the modal field overlap between different modes, as shown in Eqs. (5–7). When $\Delta k/2$ exceeds $\gamma_{FWM}\sqrt{P_1P_2}$, the gain coefficient becomes imaginary and parametric amplification ceases. The system exhibits two distinct regimes: in the low pump power regime ($g << 1$), $CE \propto g^2$, while in the high pump power regime ($g >> 1$), $CE \propto e^{2g}$, highlighting the exponential scaling advantage of operating at higher pump powers with optimal phase matching conditions.

Figure 5(b), calculated using Eq. (11), presents a theoretical sensitivity analysis demonstrating how variations in pump power distribution between the LP_{01} and LP_{02} modes impact the achievable parametric gain coefficient. This analysis is included to assess the system's robustness when the coupler's coupling ratio deviates from its designed value due to fabrication tolerances. Assuming optimal phase matching ($\Delta k = 0$), the results reveal that modest coupling deviations, such as ±20% power imbalance between P_1 and P_2, do not significantly impact the parametric gain coefficient g.

To demonstrate the flexibility of our two-mode system, we calculate the conversion efficiency for different modal combinations of the LP_{01} and LP_{02} modes by systematically scanning various pump and signal wavelengths. The corresponding idler wavelength for each pump-signal combination is determined based on energy conservation, and the total phase mismatch is calculated by combining both linear and nonlinear contributions from modal dispersion and overlap integrals. The parametric gain coefficient g and CE are subsequently obtained by combining Δk with the FWM nonlinear coefficient γ_{FWM} using Eq. (11,12), as illustrated in Fig. 6(a-d). We analyze four pump configurations for FWM: both pump waves in the LP_{01} mode (Fig. 6(a)); pump waves in both the LP_{01} and LP_{02} modes (Fig. 6(b)); both pump waves in the LP_{02} mode (Fig. 6(c)); and intramodal FWM within the LP_{01} mode (Fig. 6(d)). The simulations assume a total input power of 1 W, which is low enough to reduce the effects of nonlinear loss and yet remains compatible with our previous experimental work [37]. Based on the nanospike coupler analysis in Fig. 4, the powers coupled into the LP_{01} and LP_{02} modes are 0.84 W and 0.14 W, respectively. The main fiber section length is set to 10 mm, and while this parameter affects the CE bandwidth and absolute values, it does not influence the conversion band positions.

The bright curves in Fig. 6 represent the best-matched wavelength combinations for FWM, where different signal and idler mode combinations satisfy the phase-matching condition for each pump configuration, leading to varying conversion efficiencies. While more accurate CE values depend on loss performance of the fiber, this section focuses mainly on conversion band position. For the intramodal cases (Fig. 6(c) and Fig. 6(d)), CE is close to the pump wavelength. In contrast, when the pump and signal are in the LP_{01} mode but the idler is in the LP_{02} mode (Fig. 6(a)), the idler can be converted to the 3–5 µm range, far from the pump wavelength. Similarly, when both the pump and signal are in the LP_{02} mode, the phase-matching is determined by the single-mode dispersion curve, restricting the signal efficiency to the pump wavelength vicinity and preventing large-span wavelength conversion (3–5 µm). The most effective scenario occurs when the pump is coupled into both the LP_{01} and LP_{02} modes, while the signal is coupled into the LP_{01} mode, facilitating idler phase matching in the 3–5 µm range and extending the conversion bandwidth. A key finding is that intermodal FWM in Fig. 6(b) enables multiple conversion bands, where a single pump wavelength corresponds to several idler conversion bands. As shown in Fig. 6(b), when the pump wavelength is less than 1.94 µm, idler waves can emerge in the 3–4 µm and

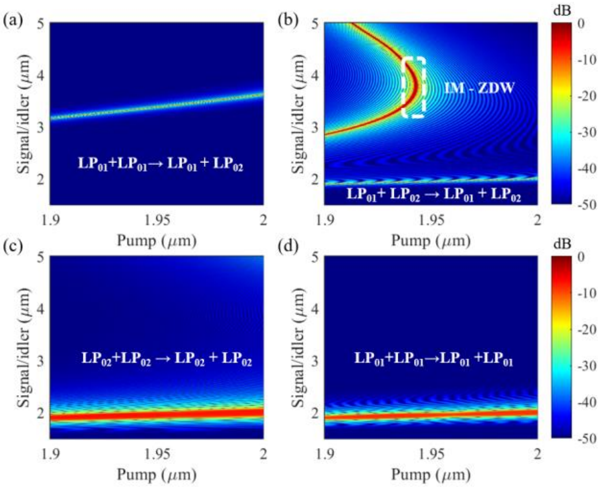

Fig. 6. Normalized CE for four FWM pump configurations between LP_{01} and LP_{02} modes as functions of pump wavelength for a 5 µm diameter SCF. (a) Both Pump1 and Pump2 in LP_{01} mode, with the signal and idler in either LP_{01} or LP_{02} mode. (b) Pump1 in LP_{01} mode and Pump2 in LP_{02} mode, with the signal and idler in different mode combinations. (c) All four waves (two pumps, signal, and idler) in LP_{02} mode. (d) All four waves in LP_{01} mode.

4–5 µm regions. Notably, these two phase-matched bands merge at the intermodal zero-dispersion wavelength (IM-ZDW), resulting in a broadband idler conversion range for a wide spectrum of signal wavelengths.

To investigate the evolution of conversion bands generated by intermodal FWM, Fig. 7(a) illustrates the conversion bandwidth at the IM-ZDW wavelength as a function of effective SCF length (fiber diameter: 5 µm, input total peak power: 1 W, coupling ratio as shown in Fig. 4(b), pump mode combination: LP_{01}-LP_{02}-LP_{01}-LP_{02}, pump wavelength: 1.94 µm). Here again we use effective fiber length to account for losses for rough estimations, as this graph primarily estimates the relationship between conversion bandwidth and transmission length. At shorter fiber lengths, the conversion band is a single, wide band; for instance, at a transmission distance of 5 mm, the 3 dB conversion bandwidth spans 3.26–3.72 µm, totaling 460 nm. As the fiber length increases, the conditions for FWM become more sensitive to phase matching, causing the single band to split into two sidebands at 3.6 µm and 3.38 µm. This behavior aligns with the data in Fig. 6(b), where the same pump wavelength corresponds to two conversion sidebands. Consequently, while the conversion efficiency significantly improves with longer fibers, the 3 dB bandwidth decreases. Nevertheless, for a length of approximately 20 mm, the sum of the conversion bandwidths of the two sidebands reaches 264 nm (with 40 nm for the signal). In the O band, a bandwidth of 40 nm is enough for wavelength division multiplexing communication with more than 50 channels.

Moreover, the pump and idler wavelength regions can be tuned further by adjusting the SCF core size. Figure 7(b) demonstrates the relationship between the IM-ZDW and the fiber core size for a 20 mm SCF. For pump lasers operating in the 1.9–2.1 µm range, SCF core diameters of 5–6 µm can effectively achieve mid-infrared wavelength conversion via intermodal schemes. The conversion bandwidth also increases with the fiber core diameter. An SCF with a 6 µm core diameter enables the broadest conversion bandwidth of up to 380 nm with a pump wavelength of 2.1 µm, which is still within the operational range of thulium-doped fiber lasers.

To evaluate the practical capability of SCFs for generating intermodal FWM, we extended the original simplified coupled equations beyond the undepleted pump approximation. In practice,

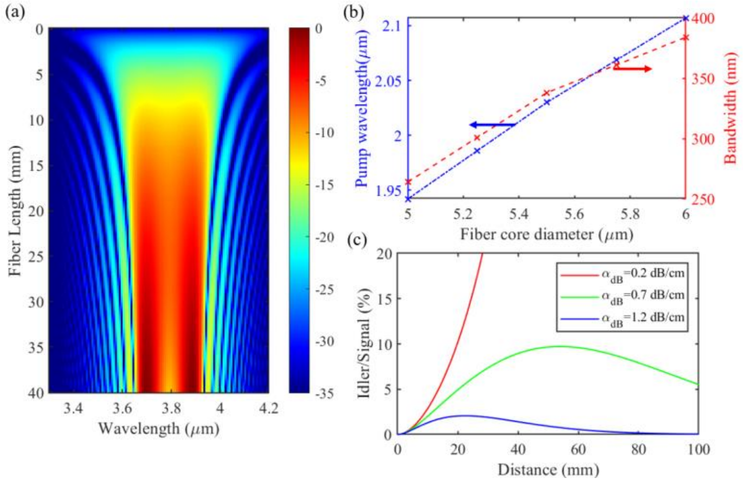

Fig. 7. (a) Normalized CE bandwidth of SCF LP_{01} and LP_{02} intermodal FWM at the IM-ZDW as a function of fiber length. (Input peak power: 1 W; coupling efficiencies for pump1, pump2, and signal are 0.83, 0.14, and 0.47, respectively; fiber diameter: 5 μm.) (b) Tuning IM-ZDW and bandwidth via core diameter for a 20 mm SCF: the blue line indicates the pump wavelength required to access the IM-ZDW (left-hand axis), while the red line shows how the 3 dB conversion bandwidth (right-hand axis) varies with changes in core diameter and pump wavelength. (c) Evolution of photon conversion efficiency for idler and signal waves with fiber length. The red, green, and blue curves correspond to pump/signal loss of 0.2, 0.7, and 1.2 dB/cm, respectively. The idler loss is set to 2 times the pump loss.

high pump intensities can lead to significant nonlinear losses from TPA, while longer fiber lengths result in non-negligible linear losses. Therefore, we incorporated both linear and nonlinear loss terms into the coupled equations to provide a more accurate evaluation of the conversion efficiency. The complete set of coupled equations is presented in the Appendix. Wavelengths dependent loss is also considered here as we use different linear loss value for pump, signal and idler waves. At wavelengths around 1.5-2 μm, reported losses are as low as 0.2 dB/cm, primarily due to Rayleigh scattering from the polycrystalline silicon grain boundaries [15,38]. In the mid-infrared region (3-5 μm), losses increase substantially due to silica cladding absorption, which depends on the modal overlap with the cladding and scales with the core diameter relative to wavelength. For our 5-6 μm core design, the theoretical cladding absorption loss remains below 0.1 dB/cm for wavelengths under 4.5 μm [16], though practical values may be higher due to OH^- contamination during fabrication. In our modeling, we adopted experimentally relevant loss values: 0.2 dB/cm for both pump and signal waves, and 0.4 dB/cm for the mid-infrared idler wave, representing two times the near-infrared loss as approximation.

To solve the coupled equations incorporating pump depletion effects, we employed the Euler method to iteratively calculate the evolution of all four wave amplitudes during fiber propagation. At each discretized step (< 100 μm), we computed the instantaneous loss and gain coefficients and their cumulative effects on the signal and idler wave amplitudes. A TPA coefficient of 1×10^{-12} m/W is assumed for the ∼1.95 μm, adopted from Ref. [39]. A nanosecond pump with 1 W average power and 1/40 duty cycle is used to avoid fiber damage. The results, presented in Fig. 7(c), demonstrate that the CE varies with fiber losses, ranging from a few percent to over 20% for a typical fiber length of 25 mm. Loss substantially impacts the idler conversion efficiency and establishes an optimal fiber length corresponding to maximum CE. Beyond this optimal length, severe pump depletion causes the gain to fall below the loss threshold, preventing further growth of idler photon numbers. We found that TPA-dominated nonlinear absorption significantly influences the net gain through both direct absorption and accompanying free carrier absorption, which can affect pump, signal, and idler waves simultaneously. Therefore, nanosecond pulse durations represent the optimal practical configuration for intermodal FWM, as they effectively suppress free carrier accumulation while remaining minimally affected by picosecond-scale group delays, ensuring negligible intermodal dispersion-induced walkoff effects.

2.4. Prospect and challenges

As we have shown, using intermodal FWM wavelength conversion in SCFs can be achieved over an unprecedented wavelength range. Although far-tuned mid-IR conversion can also be achieved using dispersion-managed glass-based fibers [18,40], a key advantage of using SCFs is their compact size along with the narrowband Raman gain they offer. The narrow Raman gain bandwidth (0.1 THz) results in spontaneous Raman noise emerging in discrete spectral bands [15,41]. This is particularly advantageous for FWM based photon pair sources used in quantum communication, where signal and idler photons operate at the single-photon level and are susceptible to interference from Raman emissions. The all-fiber integration scheme introduced here also offers great potential for the construction of robust and practical components. However, despite the clear benefits of the tapered nanospike coupler designs, they face several practical challenges in terms of their fabrication. A primary issue is the production of tapered SCFs with 10 µm cladding diameters at the splice facet. While we have successfully demonstrated robust fusion splicing of SCFs with 20 µm cladding diameters to tapered SMFs using a commercial fiber workstation [24], achieving smaller diameters requires more advanced equipment. Moreover, variations in the nanospike structure can lead to significant fluctuations in the LP_{02} mode coupling ratio, resulting in low fabrication yield. The reported insertion loss for the fundamental mode in the nanospike coupler was 4 dB, primarily attributed to the input tapered SMF not being small enough (30 µm), resulting in the excitation of unwanted cladding modes in the SCF [31]. Furthermore, since the fiber diameter is small, it is relatively soft and prone to bending. This bending can further excite unwanted cladding modes of the SCF, affecting the coupling efficiency of the nanospike. However, due to the short length of the device, this issue can be mitigated by using specialized fixtures to straighten the fiber. These challenges are part of our on-going work to standardized the fabrication processes and produce more precise SMF to SCF couplers.

3. Conclusions

In conclusion, intermodal FWM serves as a powerful complement and extension to intramodal FWM. It enables SCFs, a novel highly efficient nonlinear fiber platform, to achieve a broader range of frequency conversion into the mid-infrared region (3–5 µm). We have demonstrated the potential for efficient 3–5 µm wavelength conversion using a single thulium-doped fiber laser. A detailed model for intermodal FWM with a wavelength-dependent modal profile and losses has been developed. For a 25-mm SCF, a conversion efficiency of approximately 2-15% is attainable under representative conditions. The multimode pumping scheme can be implemented using an optimized nanospike coupler, which enables the fiberized multimode excitation of the SCF from standard silica fibers. Thus, this work lays the foundation for compact, fiberized mid-infrared parametric wavelength conversion devices, providing a detailed design blueprint for use in applications such as parametric amplification, entangled photon pair sources, and free-space communications.

Appendix

The model of this work for calculating the CE is based on the coupled equation modified from [14,36,42,43]. The underlining assumption is that the fields are under quasi continuous wave

(CW) conditions, such that all terms involving derivatives with respect to time are ignored (dispersion is negligible).

$$\frac{\partial A_1}{\partial z} = i\gamma_1[(f_{11}|A_1|^2 + 2f_{12}|A_2|^2 + 2f_{13}|A_3|^2 + 2f_{14}|A_4|^2)A_1 + 2f_{1234}A_2^*A_3A_4\exp(i\Delta kz)] - \frac{1}{2}(\alpha_{12} + \sigma_{FCA}N_c)A_1, \tag{A1}$$

$$\frac{\partial A_2}{\partial z} = i\gamma_2[(f_{22}|A_2|^2 + 2f_{21}|A_1|^2 + 2f_{23}|A_3|^2 + 2f_{24}|A_4|^2)A_2 + 2f_{1234}A_1^*A_3A_4\exp(i\Delta kz)] - \frac{1}{2}(\alpha_{12} + \sigma_{FCA}N_c)A_2, \tag{A2}$$

$$\frac{\partial A_3}{\partial z} = i\gamma_3[(f_{33}|A_3|^2 + 2f_{31}|A_1|^2 + 2f_{32}|A_2|^2 + 2f_{34}|A_4|^2)A_3 + 2f_{1234}A_1A_2A_4^*\exp(-i\Delta kz)] - \frac{1}{2}(\alpha_3 + \sigma_{FCA}N_c)A_3, \tag{A3}$$

$$\frac{\partial A_4}{\partial z} = i\gamma_4[(f_{44}|A_4|^2 + 2f_{41}|A_1|^2 + 2f_{42}|A_2|^2 + 2f_{43}|A_3|^2)A_4 + 2f_{1234}A_1A_2A_3^*\exp(-i\Delta kz)] - \frac{1}{2}(\alpha_4 + \sigma_{FCA}N_c)A_4, \tag{A4}$$

Here, A_1, A_2, A_3, A_4 are the complex amplitudes of the two pump waves, signal wave, and idler wave respectively, z is the propagation distance along the fiber, $\alpha_{12}, \alpha_3, \alpha_4$ are the linear loss coefficient of pumps, signal and idler, N_c is the free-carrier density, σ_{FCA} is the free-carrier absorption coefficient, $\gamma_m = \frac{\omega_m \tilde{n}_2}{c} + i\frac{\beta_{TPA}^m}{2}$ is the complex nonlinear coefficient for each wave. In our configuration, the pump power is much larger than signal and idler, so the terms with $|A_3|^2$ and $|A_4|^2$ can be ignored. As a quasi-CW pump is used, the free-carrier density N_c is assumed as constant, and is estimated from the rate equation adopted from [43]. The phase evolution of the pump does not affect the amplitude of signal and idler so it can be ignored.

$$\frac{\partial A_1}{\partial z} = i\gamma_1(f_{11}|A_1|^2 + 2f_{12}|A_2|^2)A_1 - \frac{1}{2}(\alpha_{12} + \sigma_{FCA}N_c)A_1, \tag{A5}$$

$$\frac{\partial A_2}{\partial z} = i\gamma_2(f_{22}|A_2|^2 + 2f_{21}|A_1|^2)A_2 - \frac{1}{2}(\alpha_{12} + \sigma_{FCA}N_c)A_2, \tag{A6}$$

$$\frac{\partial A_3}{\partial z} = i\gamma_3[(2f_{31}|A_1|^2 + 2f_{32}|A_2|^2)A_3 + 2f_{1234}A_1A_2A_4^*\exp(-i\Delta kz)] - \frac{1}{2}(\alpha_3 + \sigma_{FCA}N_c)A_3, \tag{A7}$$

$$\frac{\partial A_4}{\partial z} = i\gamma_4[(2f_{41}|A_1|^2 + 2f_{42}|A_2|^2)A_4 + 2f_{1234}A_1A_2A_3^*\exp(-i\Delta kz)] - \frac{1}{2}(\alpha_4 + \sigma_{FCA}N_c)A_4, \tag{A8}$$

In the undepleted pump regime, where the pump intensity is low and linear losses are negligible, Eq. (A5)–(A8) can be simplified to:

$$\frac{\partial A_3}{\partial z} = \frac{i\tilde{n}_2\omega_3}{c}[2(f_{31}|A_1|^2 + f_{32}|A_2|^2)A_3 + 2f_{1234}A_1A_2A_4^*\exp(-i\Delta kz)], \tag{A9}$$

$$\frac{\partial A_4}{\partial z} = \frac{i\tilde{n}_2\omega_4}{c}[2(f_{41}|A_1|^2 + f_{42}|A_2|^2)A_4 + 2f_{1234}A_1A_2A_3^*\exp(-i\Delta kz)]. \tag{A10}$$

Neglecting the phase terms of signal and idler, we obtain:

$$\frac{\partial A_3}{\partial z} = \frac{i\tilde{n}_2\omega_3}{c}2f_{1234}A_1A_2A_4^*\exp(-i\Delta kz), \tag{A11}$$

$$\frac{\partial A_4}{\partial z} = \frac{i\tilde{n}_2\omega_4}{c}2f_{1234}A_1A_2A_3^*\exp(-i\Delta kz). \tag{A12}$$

Setting $\kappa_3 = \frac{i\tilde{n}_2\omega_3}{c}2f_{1234}A_1A_2$ and $\kappa_4 = \frac{i\tilde{n}_2\omega_4}{c}2f_{1234}A_1A_2$, we obtain

$$\frac{\partial A_3}{\partial z} = \kappa_3 A_4^*\exp(-i\Delta kz), \tag{A13}$$

$$\frac{\partial A_4}{\partial z} = \kappa_4 A_3^*\exp(-i\Delta kz), \tag{A14}$$

The coupled differential equations Eq. (A13,A14) can be solved analytically using standard techniques in Ref. [36] to obtain the Eq. (9–12) in the main text.

Funding. National Natural Science Foundation of China (No. 62305043); Engineering and Physical Sciences Research Council (EP/Y008499/1, EP/P000940/1).

Acknowledgements. This study was funded by the Young Scientists Fund of the National Natural Science Foundation of China (No. 62305043), Engineering and Physical Sciences Research Council (EPSRC, GrantNos. EP/Y008499/1 and EP/P000940/1). The data that support the findings of this study will be openly available at the University of Southampton.

Disclosures. The authors declare no conflicts of interest.

Data availability. The data that support the findings of this study are openly available at the University of Southampton data repository at [44]

References

1. F. Hudelist, J. Kong, C. Liu, *et al.*, "Quantum metrology with parametric amplifier-based photon correlation interferometers," Nat. Commun. **5**(1), 3049 (2014).
2. G. Marty, S. Combrié, F. Raineri, *et al.*, "Photonic crystal optical parametric oscillator," Nat. Photonics **15**(1), 53–58 (2021).
3. L. Ledezma, R. Sekine, Q. Guo, *et al.*, "Intense optical parametric amplification in dispersion-engineered nanophotonic lithium niobate waveguides," Optica **9**(3), 303 (2022).
4. J. S. Dam, P. Tidemand-Lichtenberg, and C. Pedersen, "Room-temperature mid-infrared single-photon spectral imaging," Nat. Photonics **6**(11), 788–793 (2012).
5. N. Kuznetsov, A. Nardi, J. Riemensberger, *et al.*, "An ultra-broadband photonic-chip-based parametric amplifier," Nature **639**(8056), 928–934 (2025).
6. L. Drescher, O. Kornilov, T. Witting, *et al.*, "Extreme-ultraviolet spectral compression by four-wave mixing," Nat. Photonics **15**(4), 263–266 (2021).
7. M. Borghi and L. Pavesi, "Mitigating indistinguishability issues in photon pair sources by delayed-pump intermodal four wave mixing," Opt. Express **30**(8), 12964 (2022).
8. Y. Wang, K. D. Jöns, and Z. Sun, "Integrated photon-pair sources with nonlinear optics," Appl. Phys. Rev. **8**(1), 011314 (2021).
9. S. Paesani, M. Borghi, S. Signorini, *et al.*, "Near-ideal spontaneous photon sources in silicon quantum photonics," Nat. Commun. **11**(1), 2505 (2020).
10. J. Demas, P. Steinvurzel, B. Tai, *et al.*, "Intermodal nonlinear mixing with Bessel beams in optical fiber," Optica **2**(1), 14 (2015).
11. S. K. Turitsyn, A. E. Bednyakova, M. P. Fedoruk, *et al.*, "Inverse four-wave mixing and self-parametric amplification in optical fibre," Nat. Photonics **9**(9), 608–614 (2015).
12. H. Kishikawa, N. Goto, and L. R. Chen, "All-Optical Wavelength Preserved Modulation Format Conversion From PDM-QPSK to PDM-BPSK Using FWM and Interference," J. Lightwave Technol. **34**(23), 5505–5515 (2016).
13. Y. Zhang, C. Husko, S. Lefrancois, *et al.*, "Cross-phase modulation-induced spectral broadening in silicon waveguides," Opt. Express **24**(1), 443 (2016).
14. Y. Zhang, C. Husko, S. Lefrancois, *et al.*, "Non-degenerate two-photon absorption in silicon waveguides: analytical and experimental study," Opt. Express **23**(13), 17101 (2015).
15. M. Huang, S. Sun, T. S. Saini, *et al.*, "Raman amplification at 2.2 μm in silicon core fibers with prospects for extended mid-infrared source generation," Light: Sci. Appl. **12**(1), 209 (2023).
16. H. Ren, L. Shen, A. F. J. Runge, *et al.*, "Low-loss silicon core fibre platform for mid-infrared nonlinear photonics," Light: Sci. Appl. **8**(1), 105 (2019).
17. C. Lacava, T. Dominguez Bucio, A. Z. Khokhar, *et al.*, "Intermodal frequency generation in silicon-rich silicon nitride waveguides," Photonics Res. **7**(6), 615 (2019).
18. K. Stefańska, P. Béjot, J. Fatome, *et al.*, "High-gain far-detuned nonlinear frequency conversion in a few-mode graded-index optical fiber," Sci. Rep. **14**(1), 15872–9 (2024).
19. A. C. Peacock, P. Mehta, P. Horak, *et al.*, "Nonlinear pulse dynamics in multimode silicon core optical fibers," Opt. Lett. **37**(16), 3351 (2012).
20. H. Zhang, M. Bigot-Astruc, L. Bigot, *et al.*, "Multiple modal and wavelength conversion process of a 10-Gbit/s signal in a 6-LP-mode fiber," Opt. Express **27**(11), 15413 (2019).
21. S. M. M. Friis, I. Begleris, Y. Jung, *et al.*, "Inter-modal four-wave mixing study in a two-mode fiber," Opt. Express **24**(26), 30338 (2016).
22. R. Essiambre, M. A. Mestre, R. Ryf, *et al.*, "Experimental Investigation of Inter-Modal Four-Wave Mixing in Few-Mode Fibers," IEEE Photonics Technol. Lett. **25**(6), 539–542 (2013).
23. M. Huang, J. Ballato, and A. C. Peacock, "Semiconductor core fibres: a scalable platform for nonlinear photonics," npj Nanophotonics **1**(1), 21 (2024).
24. R. Sohanpal, H. Ren, L. Shen, *et al.*, "All-fibre heterogeneously-integrated frequency comb generation using silicon core fibre," Nat. Commun. **13**(1), 3992 (2022).
25. F. H. Suhailin, L. Shen, N. Healy, *et al.*, "Tapered polysilicon core fibers for nonlinear photonics," Opt. Lett. **41**(7), 1360 (2016).

26. D. Wu, L. Shen, H. Ren, *et al.*, “Four-Wave Mixing-Based Wavelength Conversion and Parametric Amplification in Submicron Silicon Core Fibers,” IEEE J. Sel. Top. Quantum Electron. **27**(2), 1–11 (2021).
27. E. Serrano, D. Bailleul, F. Désévédavy, *et al.*, “Towards high-power and ultra-broadband mid-infrared supercontinuum generation using tapered multimode glass rods,” Photonics Res. **13**(5), 1106 (2025).
28. H. H. Li, “Refractive index of silicon and germanium and its wavelength and temperature derivatives,” J. Phys. Chem. Ref. Data **9**(3), 561–658 (1980).
29. C. Z. Tan, “Determination of refractive index of silica glass for infrared wavelengths by IR spectroscopy,” J. Non. Cryst. Solids **223**(1-2), 158–163 (1998).
30. S. Mumtaz, R. J. Essiambre, and G. P. Agrawal, “Nonlinear propagation in multimode and multicore fibers: Generalization of the Manakov equations,” J. Lightwave Technol. **31**(3), 398–406 (2013).
31. H. Ren, O. Aktas, Y. Franz, *et al.*, “Tapered silicon core fibers with nano-spikes for optical coupling via spliced silica fibers,” Opt. Express **25**(20), 24157 (2017).
32. J. Cook, P. Roumayah, D. J. Shin, *et al.*, “Narrow linewidth 80 W tunable thulium-doped fiber laser,” Opt. Laser Technol. **146**(October 2021), 107568 (2022).
33. L. Rishøj, “Four Wave Mixing using Intermodal Nonlinearities,” Technical University of Denmark (2012).
34. H. Ren, L. Shen, D. Wu, *et al.*, “Nonlinear optical properties of polycrystalline silicon core fibers from telecom wavelengths into the mid-infrared spectral region,” Opt. Mater. Express **9**(3), 1271 (2019).
35. J. Hansryd, P. A. Andrekson, M. Westlund, *et al.*, “Fiber-based optical parametric amplifiers and their applications,” IEEE J. Sel. Top. Quantum Electron. **8**(3), 506–520 (2002).
36. G. P. Agrawal, “Chapter 10 - Four-Wave Mixing,” in *Nonlinear Fiber Optics* (Elsevier, 2006), pp. 368–423.
37. M. Huang, H. Ren, O. Aktas, *et al.*, “Fiber Integrated Wavelength Converter Based on a Silicon Core Fiber with a Nano-Spike Coupler,” IEEE Photonics Technol. Lett. **31**(19), 1561–1564 (2019).
38. M. Huang, A. N. Ghosh, C. M. Harvey, *et al.*, “Laser-drawn silicon core fibers for nonlinear photonics,” APL Photonics **10**(2), 026114 (2025).
39. Q. Lin, J. Zhang, G. Piredda, *et al.*, “Dispersion of silicon nonlinearities in the near infrared region,” Appl. Phys. Lett. **91**(2), 021111 (2007).
40. M. Evrard, E. Serrano, C. Strutynski, *et al.*, “(INVITED) Dispersion-shifted tellurite fibers for nonlinear frequency conversion,” Opt. Mater. X **15**, 100183 (2022).
41. J. H. Parker, D. W. Feldman, and M. Ashkin, “Raman scattering by silicon and germanium,” Phys. Rev. **155**(3), 712–714 (1967).
42. V. Kumar, R. K. Varshney, and S. Kumar, “Terahertz generation by four-wave mixing and guidance in diatomic teflon photonic crystal fibers,” Opt. Commun. **454**(August 2019), 124460 (2020).
43. Q. Lin, O. J. Painter, and G. P. Agrawal, “Nonlinear optical phenomena in silicon waveguides: modeling and applications,” Opt. Express **15**(25), 16604 (2007).
44. H. Ren, M. Huang, X. Liu, *et al.*, “Intermodal four-wave mixing in silicon core fibers: enabling versatile wavelength conversion in the mid-infrared range: data,” University of Southampton, 2025, https://doi.org/10.5258/SOTON/D3695.